Enhanced Anomalous Nernst Effect in the Ferromagnetic Kondo Lattice $CeCo_2As_2$

Shuyue Guan,[1,*] Weian Guo,[2,*] Pengyu Zheng,[2] Xinxuan Lin,[1] Yuqing Huang,[1] Jiawei Li,[1] Xiao-Bin Qiang,[3] Longfei Li,[1] Weiwei Xie,[4] Hai-Zhou Lu,[3] Zhiping Yin,[2,5,†] and Shuang Jia[1,6,7,‡]

[1]*International Center for Quantum Materials, School of Physics, Peking University, Beijing 100871, China*
[2]*School of Physics and Astronomy and Center for Advanced Quantum Studies, Beijing Normal University, Beijing 100875, China*
[3]*State Key Laboratory of Quantum Functional Materials, Department of Physics, and Guangdong Basic Research Center of Excellence for Quantum Science, Southern University of Science and Technology, Shenzhen 518055, China*
[4]*Department of Chemistry, Michigan State University, East Lansing, Michigan 48824, USA*
[5]*Key Laboratory of Multiscale Spin Physics (Ministry of Education), Beijing Normal University, Beijing 100875, China*
[6]*Interdisciplinary Institute of Light-Element Quantum Materials and Research Center for Light-Element Advanced Materials, Peking University, Beijing 100871, China*
[7]*Hefei National Laboratory, Hefei 230088, China*

(Received 23 June 2025; revised 6 November 2025; accepted 19 December 2025; published 23 January 2026)

The anomalous Nernst effect (ANE), generating a voltage perpendicular to a temperature gradient due to magnetization, is closely linked to the Berry curvature (BC) near the Fermi energy in topological magnets. We report an enhanced spontaneous ANE in the ferromagnetic Kondo lattice $CeCo_2As_2$, which features Kondo-screened cerium-based $4f$ moments embedded in a ferromagnetic d-electron framework. The observed large anomalous Nernst coefficient, greater than the Seebeck coefficient, is attributed to the strong BC present in the f-orbital-dominated flat bands. The enhanced ANE in $CeCo_2As_2$ serves as a signature of the Fermi energy pinning within the topological flat band, highlighting the correlation-driven topology in the Kondo lattice.

DOI: 10.1103/52tp-styb

The anomalous Nernst effect (ANE) acts as a thermoelectric counterpart to the anomalous Hall effect (AHE). It holds promise for thermoelectric devices by facilitating perpendicular current flow and improving design and performance [1,2]. Unlike the conventional Nernst effect, which necessitates an external magnetic field, the ANE in a ferromagnetic (FM) material emerges intrinsically from the magnetization, allowing for heat-to-spin and charge conversion devoid of an external magnetic field [Fig. 1(a)]. However, the anomalous Nernst coefficient ($S_{xy}^{A} = -E_y^{A}/\nabla_x T$) in conventional magnets typically measures between 0.1 and 1 $\mu V\,K^{-1}$, which is typically smaller than the Seebeck coefficient by several orders of magnitude, limiting their applicability [3–5].

It is well-established that large intrinsic AHE and ANE are distinguishing traits of topological magnets, heavily reliant on the Berry curvature (BC) distribution around the Fermi level (E_F) [6–17]. High-throughput first-principles calculations have predicted magnetic materials with notable topological structures, including nodal lines and Weyl points, where BC can yield greater S_{xy}^{A} [11,18–20]. Recent experimental work demonstrates that the large ANE is highly sensitive to E_F in the topological magnets [21,22].

In this Letter, we underscore that the f-electron Kondo effect can significantly boost the ANE by generating a narrow topological band through f-d hybridization. We conduct a comparative analysis of the magnetization, electric, and thermoelectric properties of $CeCo_2As_2$ and its isostructural, non-$4f$ analog $LaCo_2As_2$, both belonging to the RCo_2As_2 family (R = light rare earth), crystallizing in the $ThCr_2Si_2$-type structure (space group $I4/mmm$). Their magnetic characteristics are shaped by the interplay of itinerant Co d electrons and localized $R4f$ electrons [23–25]. Both $CeCo_2As_2$ and $LaCo_2As_2$ exhibit an FM ground state with the c axis as the easy axis and the Curie temperature (T_C) above 100 K [23,24]. While $LaCo_2As_2$ acts as a d-electron magnet, $CeCo_2As_2$ emerges as an FM Kondo lattice in which the Kondo effect is pivotal for Ce's $4f$ electron behavior, forming topological bands with pronounced f-orbital character [26].

Our research unveils a unique topological thermoelectric signal in the single crystals of $CeCo_2As_2$, an impressive value of S_{xy}^{A} of 7.4 $\mu V\,K^{-1}$ at 40 K. Furthermore, the values of S_{xy}^{A} surpass those of Seebeck coefficient S_{xx} across a broad temperature range, leading to an anomalous Nernst angle ($\tan\theta_{AN} = |S_{xy}^{A}/S_{xx}|$) as large as 144%. Our calculations propose that the large AHE and ANE arise from the

*These authors contributed equally to this work.
†Contact author: yinzhiping@bnu.edu.cn
‡Contact author: gwljiashuang@pku.edu.cn

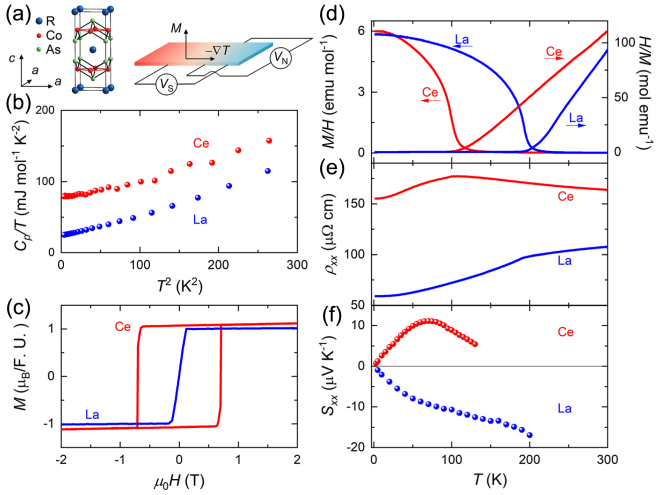

FIG. 1. Magnetization, specific heat, and transport properties of $CeCo_2As_2$ and $LaCo_2As_2$. (a) Unit cell of $CeCo_2As_2$ ($a = 4.03$ Å, $c = 10.20$ Å) and schematic illustrations of the Seebeck effect and the ANE. The Seebeck coefficient is defined as $S_{xx} = E_x/\nabla_x T$ while the anomalous Nernst coefficient is defined as $S^{\mathrm{A}}_{xy} = -E^{\mathrm{A}}_y/\nabla_x T$. The spontaneous magnetization M is along the c axis, and the heat current is applied along the a axis. The anomalous Nernst voltage $V^{\mathrm{A}}_{\mathrm{N}}$ appears perpendicular to both the magnetization and the temperature gradient. In transport measurements, the x, y, and z axes are defined along the crystallographic a, a, and c axes, respectively. (b) The low-temperature specific heat divided by the temperature $[C_p(T)/T]$ of $CeCo_2As_2$ and $LaCo_2As_2$, indicating that $C_p(T)$ can be described as $C_p(T) = \gamma T + \beta T^3$, where γT and βT^3 are the electronic and the lattice contribution, respectively. (c) The magnetic field dependence of the magnetization at 2 K. (d)–(f) The temperature dependence of the M/H and H/M curves in an external magnetic field of 0.1 T applied in the crystallographic c axis, the longitudinal electric resistivity $\rho_{xx}(T)$, and the Seebeck coefficient $S_{xx}(T)$.

pronounced BC in the f-electron characteristic bands, with multiple hybridization gaps and Weyl nodes existing within several meV of E_{F}. As the Kondo hybridization effectively pins E_{F} within these topological flat bands, the ANE is further amplified. These findings offer a unique perspective on the potential of correlated topological magnets in thermoelectric applications, providing insight into the critical interplay between the Kondo effect and electronic topology.

Single crystals of $CeCo_2As_2$ and $LaCo_2As_2$ were synthesized via a self-flux technique [25], and their thermodynamic and transport properties are presented in Fig. 1. The electronic specific heat coefficient (γ) of $CeCo_2As_2$ is measured to be 78 mJ mol^{-1} K^{-2}, which is approximately three times greater than that of $LaCo_2As_2$, indicating a significant enhancement in the effective mass of charge carriers in $CeCo_2As_2$. The temperature dependence of longitudinal resistivity $[\rho_{xx}(T)]$ of $CeCo_2As_2$ demonstrates an initial increase with decreasing temperature, culminating in a broad maximum. This behavior signifies a transition from a regime dominated by incoherent scattering of the carriers on f local moments at elevated temperatures to a state characterized by coherent scattering at lower temperatures for a Kondo lattice [27–29]. The broad maximum in $\rho_{xx}(T)$ signifies this transition with a characteristic coherence temperature ($T_{\mathrm{coh}} \sim 100$ K) for $CeCo_2As_2$. In addition, $CeCo_2As_2$ presents a positive S_{xx} with a peak at 70 K. Large and positive S_{xx} is commonly observed in cerium-based heavy fermions (HFs) due to the intricate interplay between the Kondo effect and the crystalline electric field [30]. Conversely, $LaCo_2As_2$ exhibits normal metallic behavior in its resistivity and a negative S_{xx}.

It is noteworthy that $CeCo_2As_2$ and $LaCo_2As_2$ exhibit similarities in their temperature and field-dependent magnetization. The temperature dependence of their susceptibilities aligns with Curie-Weiss behavior at elevated temperatures, with fitting yielding an effective magnetic moment $\mu_{\mathrm{eff}} = 3.6\ \mu_{\mathrm{B}}$/F.U. for $CeCo_2As_2$. This value is close to the combined μ_{eff} for $LaCo_2As_2$ ($2.9\mu_{\mathrm{B}}$/F.U.) and the Hund's rule ground state moment for the Ce^{3+} ion ($2.54\mu_{\mathrm{B}}/Ce^{3+}$), indicating a decoupling of the $4f$ local moment from itinerant electrons at high temperatures. The compounds display FM ordering at T_{C} of 190 K and 99 K, with a marked increase in magnetization observed under a weak external magnetic field below T_{C}. Furthermore, a change in the slope of the temperature-dependent resistivity is noted at T_{C}, attributed to the suppression of spin disorder scattering (see more details in Supplemental Material [31] for the determination of T_{C} and T_{coh}). The lower T_{C} of $CeCo_2As_2$ relative to T_{coh} suggests that its FM state involves collective Kondo hybridization. The nearly identical saturated magnetization of $1.0\mu_{\mathrm{B}}$/F.U. for both compounds at 2 K, as depicted in Fig. 1(c), supports the conclusion that the $4f$ local moment of the cerium atom at low temperatures is effectively quenched.

The Hall resistivity $\rho_{yx}(H)$ and the Nernst signal $S_{xy}(H)$, as illustrated in Figs. 2(b), 2(c), 2(e), and 2(f), respectively, exhibit profiles that are closely comparable to the magnetization curves, as shown in Figs. 2(a) and 2(d). Notably, $CeCo_2As_2$ displays significantly higher absolute values for both ρ_{yx} and S_{xy} than $LaCo_2As_2$. In FM conductors, the Hall resistivity can be decomposed into ordinary and anomalous contributions, expressed as $\rho_{yx} = \rho^{\mathrm{O}}_{yx} + \rho^{\mathrm{A}}_{yx}$, where ρ^{O}_{yx} and ρ^{A}_{yx} correspond to ordinary and anomalous Hall resistivities, respectively, which are linearly dependent on the external magnetic field and magnetization [59]. Similarly, the Nernst signal can also be categorized into ordinary and anomalous contributions: $S_{xy} = S^{\mathrm{O}}_{xy} + S^{\mathrm{A}}_{xy}$. Extrapolation of the high-field regions of ρ_{yx} and S_{xy} to the zero-field limit indicates that ρ^{A}_{yx} and S^{A}_{xy} of $CeCo_2As_2$ are an order of magnitude greater than those for $LaCo_2As_2$.

The temperature dependence of crucial parameters associated with anomalous effects, including the anomalous

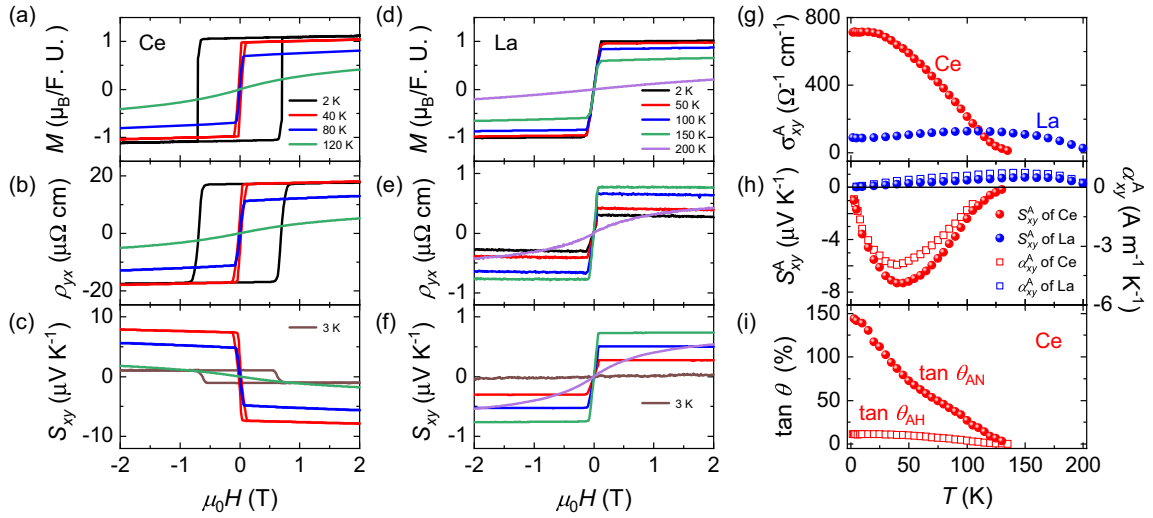

FIG. 2. Magnetic field dependence of the magnetization M, the Hall resistivity ρ_{yx}, and the Nernst coefficients S_{xy} of (a)–(c) $CeCo_2As_2$, and (d)–(f) $LaCo_2As_2$ at several representative temperatures. The temperature dependence of (g) σ_{xy}^{A} and (h) S_{xy}^{A} and α_{xy}^{A} of $CeCo_2As_2$ and $LaCo_2As_2$. (i) The temperature dependence of $\tan\theta_{AH}$ and $\tan\theta_{AN}$ of $CeCo_2As_2$.

Hall conductivity $\sigma_{xy}^{A} \simeq \rho_{yx}^{A}/\rho_{xx}^{2}$, the anomalous Nernst coefficient S_{xy}^{A}, and the anomalous Nernst conductivity $\alpha_{xy}^{A} = \sigma_{xy}^{A}S_{yy} + \sigma_{xx}S_{xy}^{A}$ for both $CeCo_2As_2$ and $LaCo_2As_2$, is summarized in Figs. 2(g) and 2(h). As the temperature decreases, σ_{xy}^{A} of $CeCo_2As_2$ increases monotonically and reaches 710 $\Omega^{-1}\,cm^{-1}$ below 20 K, significantly exceeding the maximum value observed in $LaCo_2As_2$, which is 130 $\Omega^{-1}\,cm^{-1}$ at 110 K. Consequently, anomalous Hall angle $\tan\theta_{AH} = |\sigma_{xy}^{A}/\sigma_{xx}|$ for $CeCo_2As_2$ attains its maximum of 11% at 2 K, as shown in Fig. 2(i). The values of S_{xy}^{A} for $CeCo_2As_2$ remain negative, with the absolute value increasing with temperature, peaking at 7.4 $\mu V\,K^{-1}$ around 40 K. In contrast, the values of S_{xy}^{A} for $LaCo_2As_2$ are positive and gradually rise with temperature, reaching 0.7 $\mu V\,K^{-1}$ at approximately 150 K. The observed peak value of S_{xy}^{A} for $CeCo_2As_2$ is comparable to some of the largest values reported for other topological magnets, such as 6 $\mu V\,K^{-1}$ for Co_2MnGa [8,60,61], $3-5$ $\mu V\,K^{-1}$ for $Co_3Sn_2S_2$ [9,62,63], and $6-10$ $\mu V\,K^{-1}$ for $YbMnBi_2$ [15,64]. The temperature dependence of α_{xy}^{A} of $CeCo_2As_2$ follows the profile of that of S_{xy}^{A}, with a peak value of 4.0 $Am^{-1}\,K^{-1}$, ranking among the top values reported in topological magnets [8,9,11,14–17]. In contrast, $LaCo_2As_2$ exhibits positive α_{xy}^{A} with a small peak value of 0.7 $Am^{-1}\,K^{-1}$. Notably, the absolute values of S_{xy}^{A} and S_{xx} for $CeCo_2As_2$ are comparable below its T_C, which emphasizes a significant $\tan\theta_{AN}$ of 87% at 40 K, coinciding with the maximum of S_{xy}^{A}. As shown in Fig. 2(i), the values of $\tan\theta_{AN}$ exceed 100% below 30 K, ultimately reaching 144% at the lowest measured temperature of 3 K. In comparison, the $\tan\theta_{AN}$ values for conventional bulk magnets such as Fe, Co, and Ni remain below 1% [5].

To illustrate the substantial ANE for $CeCo_2As_2$, we summarize $\tan\theta_{AN}$ and $|S_{xy}^{A}/T|$ at the lowest temperatures for various topological magnets [7–17], as depicted in Fig. 3(a). In a multiband system, S_{xx} can vanish due to electron-hole compensation at finite temperatures, in which case the $\tan\theta_{AN}$ may take arbitrarily large values [7,13,14]. However, we note that the values of $\tan\theta_{AN}$ for most of the magnets are less than 50% at low temperatures in general. Correspondingly, the values of $|S_{xy}^{A}/T|$ are less than 0.1 $\mu V\,K^{-2}$. Three f-electron compounds, $UCo_{0.8}Ru_{0.2}Al$ [14], which show great value of S_{xy}^{A} being 23 $\mu V\,K^{-1}$ at 40 K, $CeCrGe_3$ [17], and $CeCo_2As_2$, exhibit substantial values of S_{xy}^{A}/T.

It is noteworthy that these three f-electron compounds can be classified as HFs, which exhibit enhanced values of

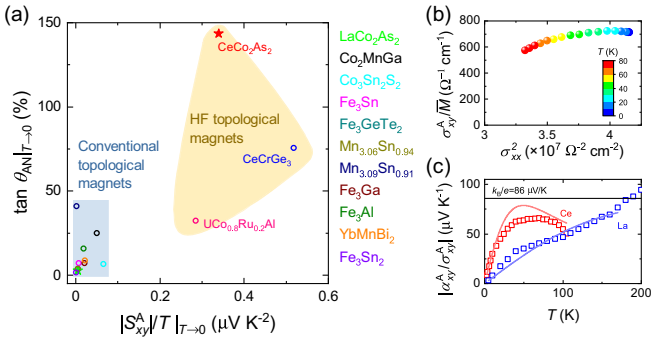

FIG. 3. (a) Summary of the data of $\tan\theta_{AN}$ and $|S_{xy}^{A}/T|$ at the lowest temperature for various topological magnets. (b) Scaling of σ_{xy}^{A} for $CeCo_2As_2$ by the normalized magnetization $\bar{M} = M(T)/M_{sat}(T = 2\ K)$ with σ_{xx}^{2}. (c) The $|\alpha_{xy}^{A}/\sigma_{xy}^{A}|$ ratio as a function of temperature for $CeCo_2As_2$ and $LaCo_2As_2$. The solid lines are the fitting curves.

γ at low temperatures. On the other hand, transport measurements on $CeCo_2As_2$ provide clear evidence of its single-band nature and reveal a large S_{xx}, making the exceptionally large $\tan\theta_{AN}$ remarkable (see details in Supplemental Material [31]). Because the large S_{xx} at low temperatures reflects the significant density of states (DOS) in HF compounds [30], the large value of $\tan\theta_{AN}$ should be ascribed to a large S^A_{xy}/T rather than a small S_{xx}, highlighting the significant ANE in HF magnets.

We scale σ^A_{xy} for $CeCo_2As_2$ divided by its normalized magnetization $\bar{M} = M(T)/M_{sat}(T = 2\ \mathrm{K})$ against σ^2_{xx} in Fig. 3(b), taking into account the variation in magnetization from 2 K to T_C. The AHE may arise from either extrinsic skew scattering contribution, leading to a quadratic relationship between the σ^A_{xy} and σ_{xx} [65], or from an intrinsic BC contribution, wherein σ^A_{xy} remains independent of σ_{xx} [59,66]. The values of $\sigma^A_{xy}/\bar{M}$ in $CeCo_2As_2$ consistently hover around 700 $\Omega^{-1}\,\mathrm{cm}^{-1}$, indicating a prevailing intrinsic contribution. It was reported that the skew scattering AHE in HFs, due to the disrupted Kondo resonance of the local moment scattering conduction electrons in a magnetic field [67,68], is characterized by a small value of $\tan\theta_{AH}$, being approximately 1% [59]. The exceptional ANE and AHE observed in $CeCo_2As_2$ necessitate a reevaluation of the role of the Kondo effect in its topological electronic structure.

To illuminate the role of $4f$ electrons in the band structure, we conducted a comparison of $LaCo_2As_2$ and $CeCo_2As_2$ utilizing the density functional theory coupled with dynamical mean-field theory (DFT + DMFT), as illustrated in Figs. 4(a) and 4(b), respectively. Significant Kondo flat bands are observed just above E_F in $CeCo_2As_2$, which are absent in $LaCo_2As_2$. The presence of these Kondo flat bands elucidates the HF properties and the significant value of $S_{xx}/T|_{T\to 0}$, as the latter is proportional to the DOS at E_F. Further analysis reveals numerous f-d hybridization gaps and Weyl points distributed within a narrow energy range near E_F (see Fig. S13 in Supplemental Material [31]).

Because direct determination of the BC is not feasible in DFT + DMFT calculations, we employed the adjusted DFT tight-binding (TB) model to capture the characteristics of Kondo flat bands and their hybridization with Co-3d bands, as shown in Fig. 4(c). A representative BC-resolved band structure with the z component Ω_z (Å^2) in the $k_z = 0 * 4\pi/c$ plane, along with those for other planes, is shown in Fig. 4(d) and the Supplemental Material [31]. Our findings demonstrate that the large σ^A_{xy} and α^A_{xy} can be attributed to the significant average BC arising from the f-d hybridization gaps and associated Weyl points. These features not only increase σ^A_{xy} [69], as the three-dimensional Kondo flat band lies near E_F, amplifying the BC contribution from occupied states across all k_z planes (Fig. S15 in Supplemental Material [31]), but also enhance α^A_{xy} by

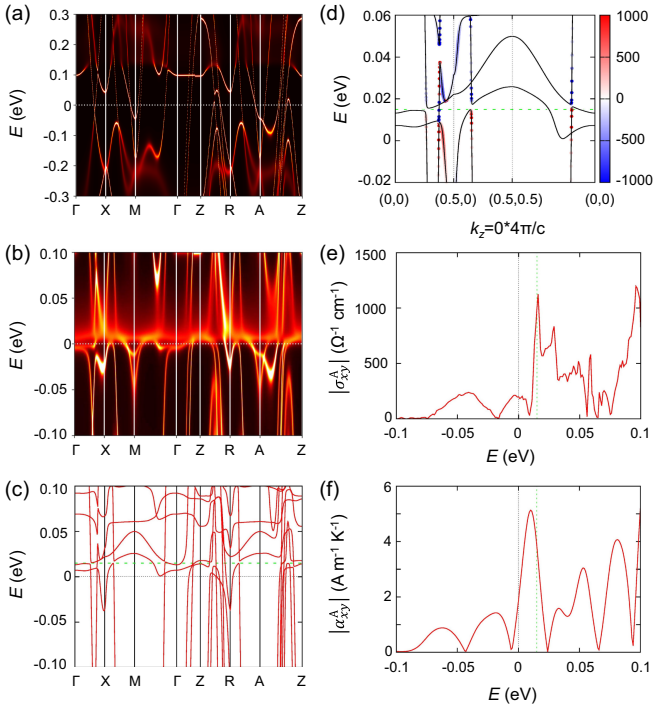

FIG. 4. DFT + DMFT band structures of (a) $LaCo_2As_2$ and (b) $CeCo_2As_2$, respectively; (c) the band structure of $CeCo_2As_2$ obtained from the adjusted DFT TB model; and, based on (c),(d) the Berry-curvature–resolved band structure with the z-component Ω_z (Å^2) in the $k_z = 0 * 4\pi/c$ plane as a representative result, (e) the calculated absolute σ^A_{xy}, and (f) the calculated absolute α^A_{xy} at $T = 50$ K. In (d)–(f), the green dashed lines represent $E = E_F + 15$ meV.

concentrating a large average BC within a narrow energy window near the E_F (Fig. S16 in Supplemental Material [31]). As shown in Figs. 4(e) and 4(f), when we set the energy at $E = E_F + 15$ meV that crosses the f flat bands, we can obtain $|\sigma^A_{xy}|$ being about 1000Ω^{-1} cm^{-1} and $|\alpha^A_{xy}|$ being about 4 Am^{-1} K^{-1} at 50 K, which agree well with the experimental values.

From the perspective of intrinsic mechanisms, the AHE and the ANE arise from electron flows that are deflected by the BC under an electric field and a thermal gradient, respectively [70,71]. These two effects are connected via the Mott relation $(\alpha^A_{xy}/T) = -(\pi^2/3)[k_B^2/e] \times \{d\sigma^A_{xy}/dE\}|_{E=E_F}$, where k_B is the Boltzmann constant and e is the electron charge. Apparently the ratio of $\alpha^A_{xy}/\sigma^A_{xy}$ for $LaCo_2As_2$ remains linear dependent on the temperature while that for $CeCo_2As_2$ deviates from the linearity above 30 K [Fig. 3(c)]. To understand the deviation from linearity, we perform the Sommerfeld expansion, with the help of the Dirac model, to modify it as $(\alpha^A_{xy}/\sigma^A_{xy}) = (eL_0T)/\{\mu[1 + (\pi^2/3)(k_BT/\mu)^2]\}$, where L_0 is the Lorentz constant and μ is the chemical potential [72]. In the limit of $k_BT \ll \mu$, the second term of the denominator is negligible, and the ratio $\alpha^A_{xy}/\sigma^A_{xy}$ exhibits a linear

temperature dependence, which is observed in $LaCo_2As_2$ and many other topological magnets [12,61,73–75]. In contrast, the second term is not negligible for $CeCo_2As_2$, indicating a small μ. We fit the measured data with the above expression, as shown by the solid curves in Fig. 3(c), to extract the μ value corresponding to $T^* = \mu/k_B = 90$ K for $CeCo_2As_2$. This value is comparable to $T_{coh} = 100$ K, indicating that the renormalized band due to the coherent Kondo hybridization is the source of the BC. On the other hand, its ultralow Fermi temperature (T_F) and T_{coh} are responsible for the breakdown of the Mott relation at elevated temperatures. As comparison, the estimated T^* for $LaCo_2As_2$ is 475 K, far above its T_C.

We now demonstrate that the low T_F is crucial for the exceptional values of $S^A_{xy}/T|_{T\to 0}$ and $\tan\theta_{AN}$ in $CeCo_2As_2$. Given that the intrinsic σ^A_{xy} is independent of electronic scattering, a low T_F leads to an elevated value of $\alpha^A_{xy}/T|_{T\to 0}$ in accordance with the Mott relation. Because the second term $\sigma_{xx}S^A_{xy}$ contributes over 90% to $\alpha^A_{xy} = \sigma^A_{xy}S_{yy} + \sigma_{xx}S^A_{xy}$ in $CeCo_2As_2$, a high value of $S^A_{xy}/T|_{T\to 0}$ is anticipated when σ_{xx} is low.

On the other hand, by applying the Mott relation in the low-temperature limit for both α^A_{xy} and α_{xx}, we derive the expression $\tan\theta_{AN}|_{T\to 0} \simeq |[(d\sigma^A_{xy}/dE)/(d\sigma_{xx}/dE)]|_{E=E_F}$, which can be compared to the formula of $\tan\theta_{AH} = |\sigma^A_{xy}/\sigma_{xx}|$. The large disparity between the two values ($\tan\theta_{AH} = 11\%$ and $\tan\theta_{AN} = 144\%$) indicates that σ^A_{xy} exhibits a markedly more sensitive response concerning energy variation than that of σ_{xx}. This result is consistent with our calculations, which demonstrate a sharp energy dependence of σ^A_{xy} near the Fermi level, as shown in Fig. 4(e).

As a measurement of the BC at E_F, a large ANE can be achieved only when the chemical potential is tuned in the vicinity of the BC "hot zones," which sometimes requires elaborate chemical substitution in topological magnets in practice [21,22]. Our calculation shows that the hybridization in $CeCo_2As_2$ spreads over the BC to an energy range of approximately tens of meV (Fig. S16 in Supplemental Material [31]). As the bandwidth is of the same magnitude, the BC is distributed over a significant portion of the flat band, leading to an enhanced ANE.

Recent studies revealed that an inversion-symmetry-breaking HF can evolve into a Weyl-Kondo semimetal state with strongly renormalized Weyl nodes residing at E_F [76–80]. Such nonmagnetic, noncentrosymmetric Kondo semimetals manifest enhanced BC due to the Kondo flat band and spontaneous Hall effect at ultralow temperatures [81]. On the other hand, our findings unveil significantly enhanced AHE and ANE in the FM Kondo lattice $CeCo_2As_2$, which serve as the fingerprint of the strong BC in topological magnets. Figures 5(e)–5(h) illustrate the pathway of the formation of this topological FM Kondo lattice and the enhancement effect of AHE and ANE, in comparison to the counterpart with only d-electron magnetism in Figs. 5(a)–5(d). As the Kondo band is generated from the hybridization between the magnetic d-electron framework and the embedded f moments, the flat band naturally involves time-reversal symmetry breaking.

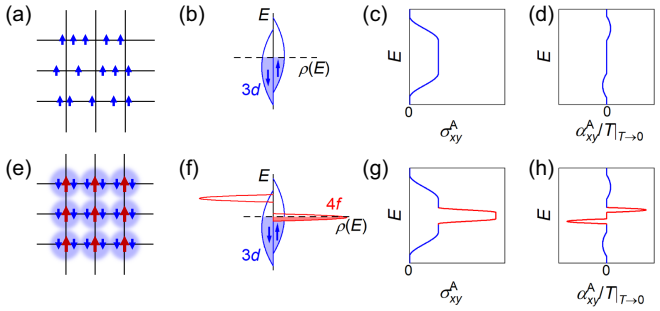

FIG. 5. Schematics of the configuration of spins, the DOS, σ^A_{xy}, and low-temperature α^A_{xy} divided by the temperature $\alpha_{xy}/T|_{T\to 0}$ in (a)–(d) the itinerant ferromagnet, and (e)–(h) the FM Kondo lattice.

A considerable value of $\tan\theta_{AN}$, and a large ratio of S^A_{xy}/T at low temperatures, can serve as indicators of low E_F and strong BC in the flat band. These observations directly point to a Kondo-pinning effect, similar to that proposed in the nonmagnetic Weyl-Kondo semimetals [79]. Those results showcase prominent anomalous transport effects of a correlated topological Kondo magnet and also highlight a thermoelectric quantum effect of a flat-band system.

Acknowledgments—This work was supported by the National Natural Science Foundation of China (Grants No. 12225401, No. 12141002, and No. 12074041), the National Key Research and Development Program of China (2021YFA1401902), Quantum Science and Technology—National Science and Technology Major Project (Grant No. 2021ZD0302600), Innovation Program for Quantum Science and Technology (No. 2021ZD0302800), and the Fundamental Research Funds for the Central Universities (Grant. No. 2243300003). The work at Michigan State University was supported by the Beckman Young Investigator Program. The DFT + DMFT calculations were carried out with the high-performance computing cluster of Beijing Normal University in Zhuhai.

Data availability—The data that support the findings of this article are openly available [82].

[1] M. Mizuguchi and S. Nakatsuji, Energy-harvesting materials based on the anomalous Nernst effect, Sci. Technol. Adv. Mater. **20**, 262 (2019).
[2] C. Fu, Y. Sun, and C. Felser, Topological thermoelectrics, APL Mater. **8**, 040913 (2020).

[3] R. Ramos, M. H. Aguirre, A. Anadón, J. Blasco, I. Lucas, K. Uchida, P. A. Algarabel, L. Morellón, E. Saitoh, and M. R. Ibarra, Anomalous Nernst effect of Fe_3O_4 single crystal, Phys. Rev. B **90**, 054422 (2014).

[4] K. Hasegawa, M. Mizuguchi, Y. Sakuraba, T. Kamada, T. Kojima, T. Kubota, S. Mizukami, T. Miyazaki, and K. Takanashi, Material dependence of anomalous Nernst effect in perpendicularly magnetized ordered-alloy thin films, Appl. Phys. Lett. **106**, 252405 (2015).

[5] T. C. Chuang, P. L. Su, P. H. Wu, and S. Y. Huang, Enhancement of the anomalous Nernst effect in ferromagnetic thin films, Phys. Rev. B **96**, 174406 (2017).

[6] D. Xiao, Y. Yao, Z. Fang, and Q. Niu, Berry-phase effect in anomalous thermoelectric transport, Phys. Rev. Lett. **97**, 026603 (2006).

[7] M. Ikhlas, T. Tomita, T. Koretsune, M.-T. Suzuki, D. Nishio-Hamane, R. Arita, Y. Otani, and S. Nakatsuji, Large anomalous Nernst effect at room temperature in a chiral antiferromagnet, Nat. Phys. **13**, 1085 (2017).

[8] A. Sakai, Y. P. Mizuta, A. A. Nugroho, R. Sihombing, T. Koretsune, M.-T. Suzuki, N. Takemori, R. Ishii, D. Nishio-Hamane, R. Arita, P. Goswami, and S. Nakatsuji, Giant anomalous Nernst effect and quantum-critical scaling in a ferromagnetic semimetal, Nat. Phys. **14**, 1119 (2018).

[9] S. N. Guin, P. Vir, Y. Zhang, N. Kumar, S. J. Watzman, C. Fu, E. Liu, K. Manna, W. Schnelle, J. Gooth, C. Shekhar, Y. Sun, and C. Felser, Zero-field Nernst effect in a ferromagnetic kagome-lattice Weyl-semimetal $Co_3Sn_2S_2$, Adv. Mater. **31**, 1806622 (2019).

[10] J. Xu, W. A. Phelan, and C.-L. Chien, Large anomalous Nernst effect in a van der Waals ferromagnet Fe_3GeTe_2, Nano Lett. **19**, 8250 (2019).

[11] A. Sakai, S. Minami, T. Koretsune, T. Chen, T. Higo, Y. Wang, T. Nomoto, M. Hirayama, S. Miwa, D. Nishio-Hamane, F. Ishii, R. Arita, and S. Nakatsuji, Iron-based binary ferromagnets for transverse thermoelectric conversion, Nature (London) **581**, 53 (2020).

[12] L. Xu, X. Li, X. Lu, C. Collignon, H. Fu, J. Koo, B. Fauqué, B. Yan, Z. Zhu, and K. Behnia, Finite-temperature violation of the anomalous transverse Wiedemann-Franz law, Sci. Adv. **6**, eaaz3522 (2020).

[13] H. Zhang, C. Q. Xu, and X. Ke, Topological Nernst effect, anomalous Nernst effect, and anomalous thermal hall effect in the Dirac semimetal Fe_3Sn_2, Phys. Rev. B **103**, L201101 (2021).

[14] T. Asaba, V. Ivanov, S. M. Thomas, S. Y. Savrasov, J. D. Thompson, E. D. Bauer, and F. Ronning, Colossal anomalous Nernst effect in a correlated noncentrosymmetric kagome ferromagnet, Sci. Adv. **7**, eabf1467 (2021).

[15] Y. Pan, C. Le, B. He, S. J. Watzman, M. Yao, J. Gooth, J. P. Heremans, Y. Sun, and C. Felser, Giant anomalous Nernst signal in the antiferromagnet $YbMnBi_2$, Nat. Mater. **21**, 203 (2022).

[16] T. Chen, S. Minami, A. Sakai, Y. Wang, Z. Feng, T. Nomoto, M. Hirayama, R. Ishii, T. Koretsune, R. Arita, and S. Nakatsuji, Large anomalous Nernst effect and nodal plane in an iron-based kagome ferromagnet, Sci. Adv. **8**, eabk1480 (2022).

[17] L. Li, S. Guan, S. Chi, J. Li, X. Lin, G. Xu, and S. Jia, Giant anomalous Hall and Nernst effects in a heavy fermion ferromagnet, arXiv:2401.17624.

[18] J. Noky, J. Gayles, C. Felser, and Y. Sun, Strong anomalous Nernst effect in collinear magnetic Weyl semimetals without net magnetic moments, Phys. Rev. B **97**, 220405 (2018).

[19] J. Noky, Q. Xu, C. Felser, and Y. Sun, Large anomalous Hall and Nernst effects from nodal line symmetry breaking in $Fe_2MnX(X = P, As, Sb)$, Phys. Rev. B **99**, 165117 (2019).

[20] J. Noky, Y. Zhang, J. Gooth, C. Felser, and Y. Sun, Giant anomalous Hall and Nernst effect in magnetic cubic Heusler compounds, npj Comput. Mater. **6**, 77 (2020).

[21] Y. Li, J. Zhou, M. Li, L. Qiao, C. Jiang, Q. Chen, Y. Li, Q. Tao, and Z.-A. Xu, Enhanced anomalous Nernst effect by tuning the chemical potential in the topological kagome ferromagnet Fe_3Sn_2, Phys. Rev. Appl. **19**, 014026 (2023).

[22] J. Liu, L. Ding, L. Xu, X. Li, K. Behnia, and Z. Zhu, Tuning the anomalous Nernst and Hall effects with shifting the chemical potential in Fe-doped and Ni-doped $Co_3Sn_2S_2$, J. Phys. Condens. Matter **35**, 375501 (2023).

[23] C. M. Thompson, X. Tan, K. Kovnir, V. O. Garlea, A. A. Gippius, A. A. Yaroslavtsev, A. P. Menushenkov, R. V. Chernikov, N. Büttgen, W. Krätschmer, Y. V. Zubavichus, and M. Shatruk, Synthesis, structures, and magnetic properties of rare-earth cobalt arsenides, RCo_2As_2 (R = La, Ce, Pr, Nd), Chem. Mater. **26**, 3825 (2014).

[24] X. Tan, Z. P. Tener, and M. Shatruk, Correlating itinerant magnetism in RCo_2Pn_2 pnictides (R = La, Ce, Pr, Nd, Eu, Ca; Pn = P, As) to their crystal and electronic structures, Acc. Chem. Res. **51**, 230 (2018).

[25] Y.-Q. Huang, P.-Y. Zheng, R. Liu, X.-T. Xu, Z.-Y. Wu, C. Dong, J.-F. Wang, Z.-P. Yin, and S. Jia, Anomalous Hall effect in ferromagnetic $LaCo_2As_2$ and ferrimagnetic $NdCo_2As_2$, Chin. Phys. B **32**, 107502 (2023).

[26] Z.-J. Cheng, Y. Huang, P. Zheng, L. Chen, T. A. Cochran, H. Hu, J.-X. Yin, X. P. Yang, M. S. Hossain, Q. Zhang, I. Belopolski, R. Liu, G. Cheng, M. Hashimoto, D. Lu, X. Xu, H. Zhou, W. Ma, G. Chang, N. Yao, Z. Yin, M. Z. Hasan, and S. Jia, Observation of Kondo lattice and Kondo-enhanced anomalous Hall effect in an itinerant ferromagnet, arXiv:2302.12113.

[27] P. Coleman, Heavy fermions: Electrons at the edge of magnetism, in *Handbook of Magnetism and Advanced Magnetic Materials* (John Wiley & Sons Ltd., New York, 2007).

[28] Y.-f. Yang, Z. Fisk, H.-O. Lee, J. D. Thompson, and D. Pines, Scaling the Kondo lattice, Nature (London) **454**, 611 (2008).

[29] S. Jang, J. D. Denlinger, J. W. Allen, V. S. Zapf, M. B. Maple, J. N. Kim, B. G. Jang, and J. H. Shim, Evolution of the Kondo lattice electronic structure above the transport coherence temperature, Proc. Natl. Acad. Sci. U.S.A. **117**, 23467 (2020).

[30] K. Behnia, D. Jaccard, and J. Flouquet, On the thermoelectricity of correlated electrons in the zero-temperature limit, J. Phys. Condens. Matter **16**, 5187 (2004).

[31] See Supplemental Material http://link.aps.org/supplemental/10.1103/52tp-styb for additional methods, data, and analyses, which include additional Refs. [32–58].

[32] G. Kotliar, S. Savrasov, K. Haule, V. Oudovenko, O. Parcollet, and C. Marianetti, Electronic structure calculations with dynamical mean-field theory, Rev. Mod. Phys. **78**, 865 (2006).

[33] K. Haule, C. Yee, and K. Kim, Dynamical mean-field theory within the full-potential methods: Electronic structure of $CeIrIn_5$, $CeCoIn_5$, and $CeRhIn_5$, Phys. Rev. B **81**, 195107 (2010).

[34] P. Blaha, K. Schwarz, G. Madsen, D. Kvasnicka, J. Luitz, R. Laskowsk, F. Tran, and L. Marks, *WIEN2k: An Augmented Plane Wave Plus Local Orbitals Program for Calculating Crystal Properties* (Technische Universität Wien, 2019), http://susi.theochem.tuwien.ac.at/reg_user/textbooks/usersguide.pdf.

[35] H. Mao and Z. Yin, Electronic structure and spin dynamics of ACo_2As_2 $(A = Ba, Sr, Ca)$, Phys. Rev. B **98**, 115128 (2018).

[36] K. Haule, Exact double counting in combining the dynamical mean field theory and the density functional theory, Phys. Rev. Lett. **115**, 196403 (2015).

[37] K. Haule, Quantum Monte Carlo impurity solver for cluster dynamical mean-field theory and electronic structure calculations with adjustable cluster base, Phys. Rev. B **75**, 155113 (2007).

[38] P. Werner, A. Comanac, L. Medici, M. Troyer, and A. Millis, Continuous-time solver for quantum impurity models, Phys. Rev. Lett. **97**, 076405 (2006).

[39] N. Marzari, A. Mostofi, J. Yates, I. Souza, and D. Vanderbilt, Maximally localized Wannier functions: Theory and applications, Rev. Mod. Phys. **84**, 1419 (2012).

[40] G. Kresse and J. Furthmüller, Efficiency of *ab-initio* total energy calculations for metals and semiconductors using a plane-wave basis set, Comput. Mater. Sci. **6**, 15 (1996).

[41] G. Pizzi *et al.*, Wannier90 as a community code: New features and applications, J. Phys. Condensed Matter **32**, 165902 (2020).

[42] Q. Wu, S. Zhang, H. Song, M. Troyer, and A. Soluyanov, WannierTools: An open-source software package for novel topological materials, Comput. Phys. Commun. **224**, 405 (2018).

[43] D. Xiao, M. Chang, and Q. Niu, Berry phase effects on electronic properties, Rev. Mod. Phys. **82**, 1959 (2010).

[44] D. Thouless, M. Kohmoto, M. Nightingale, and M. Nijs, Quantized Hall conductance in a two-dimensional periodic potential, Phys. Rev. Lett. **49**, 405 (1982).

[45] S. Shen, G. Wang, S. Jin, Q. Huang, T. Ying, D. Li, X. Lai, T. Zhou, H. Zhang, Z. Lin, X. Wu, and X. Chen, Tunable Cobalt Vacancies and Related Properties in $LaCo_xAs_2$, Chem. Mater. **26**, 6221 (2014).

[46] J. Mangez, J. Issi, and J. Heremans, Transport properties of bismuth in quantizing magnetic fields, Phys. Rev. B **14**, 4381 (1976).

[47] E. Liu *et al.*, Giant anomalous Hall effect in a ferromagnetic kagome-lattice semimetal, Nat. Phys. **14**, 1125 (2018).

[48] C. Bredl, S. Horn, and F. Steglich, Low-temperature specific heat of $CeCu_2Si_2$ and $CeAl_3$: Coherence effects in Kondo lattice systems, Phys. Rev. Lett. **52**, 1982 (1984).

[49] D. Jaccard and J. Flouquet, The normal phase of heavy fermion compounds, J. Magn. Magn. Mater. **47–48**, 45 (1985).

[50] G. Sparn, W. Lieke, U. Gottwick, F. Steglich, and N. Grewe, Low-temperature transport properties of Kondo lattices, J. Magn. Magn. Mater. **47–48**, 521 (1985).

[51] C. Ayache, J. Beille, E. Bonjour, R. Calemczuk, G. Creuzet, D. Gignoux, A. Najib, D. Schmitt, J. Voiron, and M. Zerguine, Specific heat and pressure effects in the Kondo lattice compound $CePt_2Si_2$, J. Magn. Magn. Mater. **63–64**, 329 (1987).

[52] H. Sato, J. Zhao, W. Pratt, and T. Komatsubara, Transport properties of the heavy-fermion compound $CeCu_6$ down to 14 mK, Phys. Rev. B **36**, 8841 (1987).

[53] A. Amato, D. Jaccard, J. Sierro, F. Lapierre, P. Haen, P. Lejay, and J. Flouquet, Thermopower and magneto-thermopower of $CeRu_2Si_2$ single crystals, J. Magn. Magn. Mater. **76–77** 263 (1988).

[54] A. Bhattacharjee, B. Coqblin, M. Raki, L. Forro, C. Ayache, and D. Schmitt, Anisotropy of transport properties in the Kondo compound $CePt_2Si_2$: Experiments and theory, J. Phys. (Les Ulis, Fr.) **50**, 2781 (1989).

[55] A. Lacerda, A. Visser, P. Haen, P. Lejay, and J. Flouquet, Thermal properties of heavy-fermion $CeRu_2$ Si_2 , Phys. Rev. B **40**, 8759 (1989).

[56] H. Lohneysen *et al.*, Non-Fermi-liquid behavior in a heavy-fermion alloy at a magnetic instability, Phys. Rev. Lett. **72**, 3262 (1994).

[57] A. Bianchi, R. Movshovich, I. Vekhter, P. Pagliuso, and J. Sarrao, Avoided antiferromagnetic order and quantum critical point in $CeCoIn_5$, Phys. Rev. Lett. **91**, 257001 (2003).

[58] R. Bel, K. Behnia, Y. Nakajima, K. Izawa, Y. Matsuda, H. Shishido, R. Settai, and Y. Onuki, Giant nernst effect in $CeCoIn_5$, Phys. Rev. Lett. **92**, 217002 (2004).

[59] N. Nagaosa, J. Sinova, S. Onoda, A. H. MacDonald, and N. P. Ong, Anomalous Hall effect, Rev. Mod. Phys. **82**, 1539 (2010).

[60] S. N. Guin, K. Manna, J. Noky, S. J. Watzman, C. Fu, N. Kumar, W. Schnelle, C. Shekhar, Y. Sun, J. Gooth, and C. Felser, Anomalous Nernst effect beyond the magnetization scaling relation in the ferromagnetic Heusler compound Co_2MnGa, NPG Asia Mater. **11**, 16 (2019).

[61] L. Xu, X. Li, L. Ding, T. Chen, A. Sakai, B. Fauqué, S. Nakatsuji, Z. Zhu, and K. Behnia, Anomalous transverse response of Co_2MnGa and universality of the room-temperature $\alpha_{ij}^A/\sigma_{ij}^A$ ratio across topological magnets, Phys. Rev. B **101**, 180404 (2020).

[62] L. Ding, J. Koo, L. Xu, X. Li, X. Lu, L. Zhao, Q. Wang, Q. Yin, H. Lei, B. Yan, Z. Zhu, and K. Behnia, Intrinsic anomalous Nernst effect amplified by disorder in a half-metallic semimetal, Phys. Rev. X **9**, 041061 (2019).

[63] H. Yang, W. You, J. Wang, J. Huang, C. Xi, X. Xu, C. Cao, M. Tian, Z.-A. Xu, J. Dai, and Y. Li, Giant anomalous Nernst effect in the magnetic Weyl semimetal $Co_3Sn_2S_2$, Phys. Rev. Mater. **4**, 024202 (2020).

[64] X. Guo, X. Li, Z. Zhu, and K. Behnia, Onsager reciprocal relation between anomalous transverse coefficients of an anisotropic antiferromagnet, Phys. Rev. Lett. **131**, 246302 (2023).

[65] Y. Tian, L. Ye, and X. Jin, Proper scaling of the anomalous Hall effect, Phys. Rev. Lett. **103**, 087206 (2009).

[66] S. Onoda, N. Sugimoto, and N. Nagaosa, Quantum transport theory of anomalous electric, thermoelectric, and thermal Hall effects in ferromagnets, Phys. Rev. B **77**, 165103 (2008).

[67] S. Nair, S. Wirth, S. Friedemann, F. Steglich, Q. Si, and A. J. Schofield, Hall effect in heavy fermion metals, Adv. Phys. **61**, 583 (2012).

[68] Y. feng Yang, Two-fluid model for heavy electron physics, Rep. Prog. Phys. **79**, 074501 (2016).

[69] J. Noky, J. Gooth, C. Felser, and Y. Sun, Characterization of topological band structures away from the Fermi level by the anomalous Nernst effect, Phys. Rev. B **98**, 241106 (2018).

[70] K. Behnia, *Fundamentals of Thermoelectricity* (Oxford University Press, New York, 2015).

[71] K. Behnia, What is measured when measuring a thermoelectric coefficient?, C.R. Phys. **23**, 25 (2022).

[72] X.-B. Qiang, Z. Z. Du, H.-Z. Lu, and X. C. Xie, Topological and disorder corrections to the transverse Wiedemann-Franz law and Mott relation in kagome magnets and Dirac materials, Phys. Rev. B **107**, L161302 (2023).

[73] T. Miyasato, N. Abe, T. Fujii, A. Asamitsu, S. Onoda, Y. Onose, N. Nagaosa, and Y. Tokura, Crossover behavior of the anomalous Hall effect and anomalous Nernst effect in itinerant ferromagnets, Phys. Rev. Lett. **99**, 086602 (2007).

[74] Y. Pu, D. Chiba, F. Matsukura, H. Ohno, and J. Shi, Mott relation for anomalous Hall and Nernst effects in $Ga_{1-x}Mn_x$ As ferromagnetic semiconductors, Phys. Rev. Lett. **101**, 117208 (2008).

[75] X. Xu, J.-X. Yin, W. Ma, H.-J. Tien, X.-B. Qiang, P. V. S. Reddy, H. Zhou, J. Shen, H.-Z. Lu, T.-R. Chang, Z. Qu, and S. Jia, Topological charge-entropy scaling in kagome chern magnet $TbMn_6Sn_6$, Nat. Commun. **13**, 1197 (2022).

[76] H.-H. Lai, S. E. Grefe, S. Paschen, and Q. Si, Weyl–Kondo semimetal in heavy-fermion systems, Proc. Natl. Acad. Sci. U.S.A. **115**, 93 (2018).

[77] S. E. Grefe, H.-H. Lai, S. Paschen, and Q. Si, Weyl–Kondo semimetal: Towards control of Weyl nodes, in *Proceedings of the International Conference on Strongly Correlated Electron Systems (SCES2019)* (The Physical Society of Japan, Tokyo, 2020), p. 011013.

[78] S. Paschen and Q. Si, Quantum phases driven by strong correlations, Nat. Rev. Phys. **3**, 9 (2021).

[79] L. Chen, C. Setty, H. Hu, M. G. Vergniory, S. E. Grefe, L. Fischer, X. Yan, G. Eguchi, A. Prokofiev, S. Paschen, J. Cano, and Q. Si, Topological semimetal driven by strong correlations and crystalline symmetry, Nat. Phys. **18**, 1341 (2022).

[80] J. G. Checkelsky, B. A. Bernevig, P. Coleman, Q. Si, and S. Paschen, Flat bands, strange metals and the Kondo effect, Nat. Rev. Mater. **9**, 509 (2024).

[81] S. Dzsaber, X. Yan, M. Taupin, G. Eguchi, A. Prokofiev, T. Shiroka, P. Blaha, O. Rubel, S. E. Grefe, H.-H. Lai, Q. Si, and S. Paschen, Giant spontaneous Hall effect in a nonmagnetic Weyl–Kondo semimetal, Proc. Natl. Acad. Sci. U.S.A. **118**, e2013386118 (2021).

[82] S. Guan, Source data for the manuscript "Enhanced Anomalous Nernst effect in the ferromagnetic Kondo lattice CeCo2As2", 2025, 10.18170/DVN/K1KRHJ.